PHYSICAL REVIEW A VOLUME 60, NUMBER 6 DECEMBER 1999

Determination of the scattering lengths of ^{39}K from 1_u photoassociation line shapes

C. J. Williams, E. Tiesinga,* and P. S. Julienne
Atomic Physics Division, National Institute of Standards and Technology, Gaithersburg, Maryland 20899-8423

H. Wang, W. C. Stwalley, and P. L. Gould
University of Connecticut, Storrs, Connecticut 06269-3046

(Received 25 May 1999)

We report threshold scattering properties for $^{39}\mathrm{K}(f=1)$ atoms obtained from analysis of experimental photoassociation spectra of the purely long-range $^{39}\mathrm{K}_2$ 1_u state. The existence of hyperfine structure in the excited K_2 1_u state and a knowledge of the Hamiltonian structure for two colliding ground state alkali atoms enables us to obtain information on the sign and magnitudes of certain scattering lengths for ground state collisions. Analysis of the experimental photoassociation line shapes shows that the ^{39}K scattering lengths are between -3.2 and $+0.8$ nm ($-60a_0$ and $+15a_0$, where $1a_0=1$ a.u.$=0.052\,917\,7$ nm) for the $a\,^3\Sigma_u^+$ molecular state, between $+4.8$ and $+12$ nm ($+90a_0$ and $+230a_0$) for the $X^1\Sigma_g^+$ state, and between -7.9 and $+1.1$ nm ($-150a_0$ and $+20a_0$) for collisions of two $f=1,m=-1$ atoms. [S1050-2947(99)03612-4]

PACS number(s): 32.70.$-$n, 32.80.Pj, 33.15.Pw, 33.20.Vq

I. INTRODUCTION

The development of laser cooling, high resolution photoassociation spectroscopy, and more recently Bose-Einstein condensation has resulted in an increasing body of information on the alkali dimer molecular potentials and ground state scattering lengths. The first attempts to determine the scattering lengths of K were based on the inversion of bound state spectroscopic data in order to obtain very accurate $X^1\Sigma_g^+$ and $a^3\Sigma_u^+$ potentials which could then be used for calculating scattering lengths of K [1,2]. Although this procedure is fairly successful when applied to Li [3,4] where the mass is relatively small, it has not been successful in any of the heavier alkali systems. Recent history shows that careful experimental measurements of elastic collision rates, measurements of the last bound states, and/or a joint experimental-theoretical analysis of photoassociation spectra are typically required to obtain accurate scattering lengths.

The first ultracold high resolution photoassociation experiments were done using Na in a magneto-optical trap [5] and Rb in a far off resonance trap [6]. This was followed by experiments in Li [7], K [8–10], and Cs [11,12]. Careful analysis of high resolution photoassociation spectral intensities and line shapes proved invaluable in refining the early values of the scattering lengths of Na [13] and of the ^{85}Rb and ^{87}Rb isotopes [14]. The measurements in Rb have also benefited from accurate elastic collision measurements [15] and practically all the scattering length information on Cs comes from various collision measurements with the exception of the recent analysis of the 0_g^- photoassociation spectra [11].

Ultracold photoassociation results from the resonant absorption of light by two colliding ground state atoms, in our case $^{39}\mathrm{K}(f=1)$ atoms, to form an excited bound molecular state. Photoassociation is useful in obtaining scattering lengths since the Franck-Condon factors which describe the optical absorption process provide a sensitive measure of the nodal properties and amplitude of the ground state continuum wave function [6,16,17]. In the present study of ^{39}K we analyze line shapes and intensity patterns resulting from the excitation of rovibrational hyperfine levels of states with 1_u electronic symmetry which adiabatically correlate to the $4P_{3/2}+4S$ separated atom limit. The 1_u state is a Hund's case (c) adiabatic potential curve that has a purely long range potential well created by the spin-orbit avoided crossing of the repulsive $^3\Sigma_u^+$ and $^1\Pi_u$ states with the attractive $^3\Pi_u$ state [18]. This purely long-range state was first predicted by Stwalley and collaborators [19], first observed in $^{39}\mathrm{K}_2$ under the same tutelage [10] and subsequently observed in Cs [20]. A companion paper [21] provides a similar analysis of the purely long range 0_g^- state which results from a spin-orbit avoided crossing between the repulsive $^3\Pi_g$ and attractive $^3\Sigma_g^+$ states [18,19].

II. EXPERIMENT

The experimental setup has previously been described in detail [8]. Briefly, a high density "dark spot" vapor cell magneto-optical trap confines a sample of 10^7 $^{39}\mathrm{K}(f=1)$ atoms with density $>10^{11}$ atoms/cm^3 and a temperature ≈ 350 μK. The trapping and repumping laser beams are provided by a single mode tunable ring Ti:sapphire laser at 766.5 nm and with a total power ≈ 300 mW. The photoassociation is induced by a Ti:sapphire laser with tunable frequency ν_1 and a typical intensity of <50 mW/cm^2, sufficiently low that power broadening and Stark shifts of the lines are negligible. The weakly bound 1_u state, $D_e=16.2$ GHz, is not easily observed with the trap loss detection technique commonly used in photoassociation experiments. This is because the lowest vibrational levels of this state have local kinetic energies that are relatively small and as a result, when these levels undergo bound-free radiative decay, the resulting atoms typically lack sufficient kinetic

---

*Permanent address: Department of Chemistry and Biochemistry, University of Maryland, College Park, MD 20742.

energy to escape from the trap. To counter this, a second laser is introduced in order to produce an ionization signal.

In summary, the colliding ground-state atomic pairs are excited by the photoassociation photon at frequency ν_1 to a bound vibrational level of the 1_u state dissociating to the $\mathrm{K}(4^2P_{3/2})+\mathrm{K}(4S)$ atomic asymptote. A second (yellow) photon at ν_2 with $\lambda \approx 583$ nm and a typical intensity ≈ 10 W/cm^2 excites the molecule to a highly excited molecular resonance below the $\mathrm{K}(5D)+\mathrm{K}(4S)$ limit. The highly excited molecules either autoionize or are photoionized by another photon of frequency ν_1 or ν_2. A channeltron multiplier is used to collect ions generated by the two processes. The laser beam at ν_2 is alternated in time with the trapping beam using two acousto-optic modulators in order to avoid the direct production of the atomic K^+ ions from the atomic $4^2P_{3/2}$ state populated by the trapping laser. High-resolution spectra of the 1_u levels $v=0-7$ are observed by monitoring the ion production while scanning ν_1 with ν_2 fixed at a broad double-resonance peak with a linewidth of ≈ 1 GHz and no rotational structure, similar to the experiment with the $^{39}\mathrm{K}_2$ 0_g^- state [22]. The resolved spectra of the vibrational levels cannot be interpreted with a simple rotational analysis. Instead, the features are described by strong rotation-hyperfine couplings even for the $v=0$ level of the 1_u state. The binding energies of the rotational-hyperfine levels have been accurately measured with a 0.060 GHz uncertainty relative to the barycenter (hyperfine degeneracy-weighted center) of the $\mathrm{K}(4^2P_{3/2})+\mathrm{K}(4^2S)$ atom limit and have been used to determine precisely the molecular constants and rotation-hyperfine couplings of the 1_u state [10].

III. THEORY

Photoassociation line shapes and intensities have previously been used to obtain the scattering lengths of both Na [13] and Rb [14]. The basic approach used here is similar to the analysis used in obtaining the Na scattering lengths from the $^{23}\mathrm{Na}_2$ 0_g^- photoassociation spectra [13]. The basis of that analysis is the line shape expression for the free to bound transition for a laser of frequency ω and temperature T given by

$$S(\omega,T,v)=\sum_{F'p'I'\beta,Fp\ell f\alpha} n_\alpha(2F'+1) \int_0^\infty dE\, e^{-E/k_BT}\frac{\gamma_o|\langle \phi^{F'v}_{p'I'\beta}|\hbar\Omega|\Psi^{E(+)}_{Fp\ell f\alpha}\rangle|^2}{(E+\hbar\omega-E^{F'v}_{p'I'\beta})^2+(\gamma_v/2)^2}. \tag{1}$$

This expression is a Lorentzian profile convolved with a thermal distribution of ground state collision energies E [23]. The denominator is a standard resonance denominator describing a transition from an incident continuum wave function of energy E to a bound state of energy $E^{F'v}_{p'I'\beta}$ with an excited state natural linewidth of γ_v. The numerator consists of a Boltzmann factor describing the thermal collision ensemble and a matrix element that consists of three major pieces: the ground state wave functions $|\Psi^{E(+)}_{Fplf\alpha}\rangle$, the excited state wave functions $|\phi^{F'v}_{p'I'\beta}\rangle$, and the molecular Rabi matrix Ω that results from the interaction of the electronic transition dipole moment with the laser. The resulting line would produce a standard Voigt profile if the matrix element in the numerator was independent of E. However, because of the low collision energies the matrix element in the numerator possesses an additional energy dependence due to the Wigner threshold law applicable to $|\Psi^{E(+)}_{Fp\ell f\alpha}\rangle$. In the above expression primed quantities are used to denote excited state labels, where the quantum numbers are F for the total angular momentum of the system, I for the nuclear spin, p for the parity, f for the total hyperfine angular momentum $\vec{f}=\vec{f}_a+\vec{f}_b$ of the two atoms a and b [24] and ℓ for the mechanical rotation of the two atoms about their center of mass. Any other quantum label needed to define the ground and excited state are designated by α and β, respectively, and n_α describes the fraction of ground state diatoms in state α. The parameter γ_o describes the rate of photoionization to all detection channels.

The expression for the line shape is essentially identical to that used in the $^{23}\mathrm{Na}_2$ 0_g^- analysis and in the companion paper on $^{39}\mathrm{K}_2$ 0_g^- [21], with the exception that the 1_u rovibrational levels are not states of good angular momentum J', but are instead labeled by F' and I' where $\vec{F}'=\vec{J}'+\vec{I}'$ is the total angular momentum including the nuclear spin I'. Dipole selection rules for Ω insure that $F'=\{F,F\pm 1\}$ and $p=-p'$. Finally Eq. (1) includes a sum over all ground state parameters and all excited state levels that contribute intensity to a given experimental feature.

In order to model the photoassociation line shapes it is necessary to know the experimental temperature T and to calculate each of the transition dipole matrix elements $\langle \phi^{F'v}_{p'I'\beta}|\hbar\Omega|\Psi^{E(+)}_{Fp\ell f\alpha}\rangle$. For the latter, we need to calculate the excited state eigenvalues and eigenfunctions, the ground state wave functions, and the molecular transition dipole operator responsible for providing optical coupling between the ground and excited states. The theory and computational tools needed for each of these elements are briefly described in the remainder of Sec. III.

The wave functions are expressed in a coupled-channels expansion with R-dependent coefficients. The basis set includes all degrees of freedom associated with electronic orbital and spin angular momentum, the rotation of the internuclear axis, and nuclear spin. We also make use of reduced basis sets that exclude some degrees of freedom for the purpose of classifying states and developing approximations. For example, it is convenient to make use of the various Hund's coupling cases for molecular angular momentum. However, it should be kept in mind that our final calculations include all degrees of freedom.

A. Excited state

The long-range interactions between a ^2S ground state atom and an identical excited ^2P atom in the absence of nuclear rotation and hyperfine interactions is described by Movre and Pichler [18]. In this model it suffices to describe the electronic component of the total molecular wave functions, which of course describes nuclear as well as electronic degrees of freedom. The model finds an adiabatic correlation for the electronic degrees of freedom given by the interplay between the long-range molecular multipole potential, that includes $1/R^3$ resonant-dipole, $1/R^6$ and higher-order polarization interactions and retardation contributions [25], and the atomic spin-orbit Hamiltonian of the ^2P atom. At internuclear separations R, where the multipole interactions dominate, the good quantum numbers are the projection Λ of the electronic orbital angular momentum $\vec{L}=\vec{l}_a+\vec{l}_b=\vec{l}_a$ $(\vec{l}_b=0)$ and the total electron spin $\vec{S}=\vec{s}_a+\vec{s}_b$. At large internuclear separations, where the atomic Hamiltonian dominates, the good quantum numbers are $\vec{j}_a=\vec{l}_a+\vec{s}_a$ for the ^2P atom and $\vec{j}_b=\vec{s}_b$ for the ^2S atom. The notation $l_a=1$, $l_b=0$, $s_a=s_b=1/2$, where the subscripts a and b label the P and S atoms, respectively, is used throughout.

At short internuclear separations the multipole interaction dominates and gives rise to (nonrelativistic) adiabatic Born-Oppenheimer (ABO) potentials labeled by $^{2S+1}\Lambda_\sigma$, where Λ is the absolute value of the projection of L on the internuclear axis. The label $\sigma=g,u$ denotes the symmetry of the electronic wave function under inversion of the electrons through the center of charge [26]. The multipole interaction is diagonal in the ‘‘molecular’’ basis $|\Lambda S\Sigma\rangle_\sigma$ with Σ the projection of S on the internuclear axis. At large internuclear separations the atomic spin-orbit interaction dominates and this part of the Hamiltonian is diagonal in the body-fixed atomiclike basis $|(j_aj_b)j\Omega\rangle_\sigma$, where $\vec{j}=\vec{L}+\vec{S}=\vec{j}_a+\vec{j}_b$, and $\Omega=\Lambda+\Sigma$. Within the Movre-Pichler model, which includes only the long range multipole and atomic spin-orbit interactions, the electronic states with common Ω ($\Omega^\pm$ when $\Omega=0$) and σ define independent subspaces.

At all internuclear separations adiabatic potentials can be obtained by diagonalizing a potential matrix labeled by Ω_σ. At small and large R, these adiabatic potentials approach the limiting cases characterized by the respective $|\Lambda S\Sigma\rangle_\sigma$ and $|(j_aj_b)j\Omega\rangle_\sigma$ basis sets. For the 1_u subspace an extended Movre-Pichler Hamiltonian that includes retardation and dispersion can be written in the molecular basis as

$$\begin{array}{c} \\ {}^3\Sigma \\ {}^1\Pi \\ {}^3\Pi \end{array} \begin{array}{c} \begin{array}{ccc} \quad{}^3\Sigma\quad & \quad{}^1\Pi\quad & \quad{}^3\Pi\quad \end{array} \\ \begin{pmatrix} V_{^3\Sigma}-\Delta/3 & -\Delta/3 & \Delta/3 \\ -\Delta/3 & V_{^1\Pi}-\Delta/3 & \Delta/3 \\ \Delta/3 & \Delta/3 & V_{^3\Pi}-\Delta/3 \end{pmatrix} \end{array}. \tag{2}$$

In the asymptotic region, where exchange interactions are negligible, the potentials V_γ in Eq. (2) can be written as

$$V_{^3\Sigma}=\frac{2C_3}{R^3}f^{\Sigma}(R)-\frac{C_6^{\Sigma}}{R^6}, \tag{3a}$$

$$V_{^1\Pi}=\frac{C_3}{R^3}f^{\Pi}(R)-\frac{C_6^{\Pi}}{R^6}, \tag{3b}$$

$$V_{^3\Pi}=-\frac{C_3}{R^3}f^{\Pi}(R)-\frac{C_6^{\Pi}}{R^6}, \tag{3c}$$

where the C_3 coefficient is extracted from experimental photoassociation measurements of the K_2 0_g^- state [9] and the C_6^{Σ} and C_6^{Π} coefficients are taken from theoretical calculations of dispersion coefficients [27]. We also include the C_8 coefficients of Ref. [27], but their value is not crucial to our analysis. The quantity

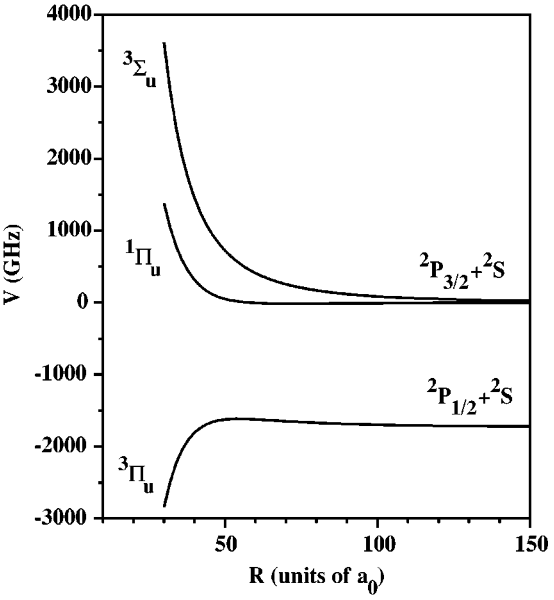

FIG. 1. The adiabatic 1_u potentials of ^{39}K as a function of internuclear separation. The short-range correlation to $^{2S+1}\Lambda_u$ Born-Oppenheimer potentials and the long-range correlation to $^2P_j+^2S$ atomic limits is given. The middle adiabatic potential corresponds to the purely long-range 1_u potential.

$$f^{\Lambda}(R)=\left[1-\delta_{\Lambda,\Pi}\left(\frac{R}{\lambda\!\!\!^{-}}\right)^2\right]\cos\left(\frac{R}{\lambda\!\!\!^{-}}\right)+\frac{R}{\lambda\!\!\!^{-}}\sin\left(\frac{R}{\lambda\!\!\!^{-}}\right), \tag{4}$$

accounts for retardation of the C_3 resonant dipole interaction where $\delta_{\Lambda,\Pi}=1$ if $\Lambda=\Pi$ and 0 otherwise and $\lambda\!\!\!^{-}$ is the wavelength of the K$(4S)$ to K$(4P)$ transition divided by 2π. This wavelength is defined with respect to the barycenter of the K$(4S)$ to K$(4P)$ transition.

Diagonalization of the potential matrix in Eq. (2) produces three adiabatic potentials of $\Omega_\sigma=1_u$ symmetry. Because this diagonalization is R dependent where the potentials V_γ are of a magnitude similar to Δ, the adiabatic electronic eigenstates are a R-dependent linear combination of the $|\Lambda S\Sigma\rangle_\sigma$ or alternatively $|(j_aj_b)j\Omega\rangle_\sigma$ states. For the 1_u states the three R-dependent eigenstates in terms of the $|(j_aj_b)j\Omega\rangle_\sigma$ basis are

$$|1_\sigma,i;R\rangle=a_{i\sigma}(R)|(1/2\,1/2)11\rangle_\sigma+b_{i\sigma}(R)|(3/2\,1/2)11\rangle_\sigma+c_{i\sigma}(R)|(3/2\,1/2)21\rangle_\sigma, \tag{5}$$

where the label $i=1$, 2, or 3 is an energy ordered index to the adiabatic potentials (also called adiabats) and $a_{i\sigma}^2+b_{i\sigma}^2+c_{i\sigma}^2=1$. Figure 1 shows the three long-range adiabatic potentials for the ^{39}K 1_u symmetry, including small R molecular and large R atomic correlations. Notice that $1a_0=0.052\,917\,724\,9$ nm. The electronic eigenfunction of the lowest adiabat of Fig. 1 reduces to $|1_u,1;R\rangle=|(1/2\,1/2)11\rangle_g$ in the limit that the binding energy is small compared to the spin-orbit splitting. Similarly, the second and third adiabats become orthogonal linear combinations of $|(3/2\,1/2)11\rangle_u$ and $|(3/2\,1/2)21\rangle_u$. The second adiabat is the purely long-range 1_u state on which we will focus for the remainder of this paper. The R-dependent eigenstates in the molecular basis can be found by applying the unitary transformation that connects the $|\Lambda S\Sigma\rangle_\sigma$ basis to the atomiclike basis $|(j_a j_b) j\Omega\rangle_\sigma$.

It is worth connecting the electronic-spin basis states with the usual Hund's coupling schemes for molecular angular momenta. It must be emphasized that Hund's classification also involves nuclear rotation. Nevertheless, within the Movre-Pichler model we often make the connection with Hund's classification. The molecular basis $|\Lambda S\Sigma\rangle_\sigma$ corresponds with Hund's case (a), where Λ, S, Σ, and σ are individually good quantum numbers. The atomiclike body-fixed basis $|(j_a j_b) j\Omega\rangle_\sigma$ and the Hund's case (c) adiabatic basis $|\Omega_\sigma, i; R\rangle$ both correspond to body-fixed basis sets where the projections Ω and σ are good quantum numbers.

Even within this extended Movre-Pichler model it is not possible to fully describe the mechanical rotation and hyperfine interactions. This is because off-diagonal coriolis/rotational forces cause mixing between states of identical $\sigma=u$ Hund's case (c) symmetries but where Ω differs by 0, ± 1, while off-diagonal hyperfine interactions couple the g and u Hund's case (c) symmetries. However, due to the absence of crossings and nearly degenerate parallel curves of other Hund's case (c) symmetries, the purely long range 1_u state is isolated. Consequently in addition to the extended Movre-Pichler Hamiltonian described by Eq. (2) it is an excellent approximation to include only hyperfine and rotational/Coriolis interactions within the 1_u manifold [10]. Although the addition of hyperfine and rotational interactions to the extended Movre-Pichler model is sufficient to reproduce [10] the 1_u rotational and hyperfine level positions, the actual level positions used in this paper follow from diagonalization of the full Hamiltonian including the nuclear kinetic energy operator and all Hund's case (c) symmetries Ω_σ and hyperfine spin states that correlate to the $\mathrm{K}(4^2P)+\mathrm{K}(4^2S)$ asymptotic limit. Since deviations between Ref. [10] and the more exact calculations are very small (on the order of 1 MHz), we denote each rotation/hyperfine level of a 1_u vibrational level by the conserved quantum numbers given by the model of Ref. [10]. These labels are the total angular momentum F' and total nuclear spin I'. Symmetry under interchange of the identical nuclei further ensures that even (odd) $I' 1_u$ levels have odd (even) parity p' and hence are formed from a linear superposition of even (odd) partial waves ℓ.

The excited bound-state wave functions and eigenvalues for the rotating molecule with hyperfine structure are calculated numerically for the set of states labeled by F', parity, and even (odd) ℓ by using an iterative eigenvalue solver on a shifted inverse Hamiltonian or Greens function. These eigenfunctions are used below in forming the transition dipole matrix elements in the numerator of Eq. (1). The number of spatial grid points needed is reduced by an order of magnitude by using a mapped Fourier grid representation that takes advantage of the long range R^{-3} potential characteristic of these problems. For a full description of the technique see Tiesinga *et al.* [28].

For the long range part of the excited state potentials we use an experimentally determined C_3 coefficient [9] and the C_6 and C_8 coefficients of Marinescu *et al.* [27]. At intermediate internuclear separations these long range potentials are smoothly fit onto the eight short-range ABO potentials. In practice at $R=30a_0$ well inside the inner turning point of the long-range 1_u potential curve, we replace all eight ABOs with a hard wall. The exact nature of the short-range potential does not alter the eigenvalues and eigenfunctions for the pure long range 1_u state of interest, since the observed rovibrational levels of the 1_u do not couple to states of other Ω_σ symmetry. However, the same comment is not necessarily valid for eigenfunctions and eigenvalues of other symmetries. Note, also that the usual rotational/Coriolis Hamiltonian found in standard diatomic textbooks [29] is not valid within the Movre-Pichler model since it asymptotically results in spurious couplings between the basis sets $|(j_a j_b) j\Omega\rangle_\sigma$ as $R\rightarrow\infty$.

B. Ground state

The ground state scattering wave functions needed to evaluate the transition dipole matrix element in Eq. (1) are calculated using standard close coupling methods including hyperfine interactions [30]. The short-range $X^1\Sigma_g^+$ and $a^3\Sigma_u^+$ potentials are RKR potentials obtained from inversion of spectroscopic data. However, unlike Refs. [1,2] we treat these potentials as only approximate representations of the true potentials. The singlet and triplet ground state potentials are smoothly fit onto a long range potential which includes both dispersion and exchange. For two $K(4S)$ ground state atoms we nominally adopt the long range dispersion coefficient C_6 of 3812.5 Hartree a_0^6 (1 Hartree $=4.359\,748\,2\times10^{-18}$ J) [27]. Finally a half-harmonic oscillator is added smoothly from the bottom of the well onto the inner wall of the potential. Altering the strength of the half-harmonic oscillator allows for a smooth adjustment of the phase due to the inner part of the approximate singlet and triplet potentials.

It should be noted that adding a half-harmonic oscillator is by no means unique. Any adjustment of the potential for internuclear separations where the $X^1\Sigma_g^+$ and $a^3\Sigma_u^+$ potentials are widely separated and much deeper in energy than the atomic hyperfine splittings is acceptable. Then alternative approaches to changing the shape (or adjusting the phase) of the potentials will only provide different ''artificial'' parameter sets that give identical accumulated phases for the inner part of the approximate potentials. More importantly these alternative changes will not significantly modify the energy dependence of accumulated phases.

Combining the above potentials with a spin-spin dipole interaction, mechanical rotation and the atomic hyperfine interactions provides us with a complete set of coupled differential equations. Mies *et al.* [31] discuss the underlying symmetries of two ground state alkali atoms in the absence of an external magnetic field. In such a case F, the total angular momentum of the system is a good quantum number and a Hamiltonian with a finite number of spin channels can be set up. Notice that $\vec{F}=\vec{\ell}+\vec{f}$, where ℓ is the mechanical rotation angular momentum and $\vec{f}=\vec{f}_a+\vec{f}_b$ is the total hyperfine angular momentum of the two atoms. In the absence of the weak spin-spin dipole interactions f and ℓ are also good quantum numbers. Additionally, because of identical atom symmetry two ground state atoms with $f_a=f_b=1$ can only couple to $f=\{0,2\}$ for $\ell=\{0,2,4,\ldots\}$ and to $f=1$ for $\ell=\{1,3,\ldots\}$.

For two ^{39}K atoms colliding at a temperature of 400 μK we expect that only $\ell=\{0,1\}$ can contribute significantly to the collisions in the absence of shape resonances. The d-wave $(\ell=2)$, which possesses a 1500 μK barrier, would be expected to have a negligible role. However, as described below, the existence of a d-wave shape resonance can modify this simplistic view. It can easily be verified that the $f=\{1,2\}$ Hamiltonians consist of three (strongly) exchange coupled channels with one channel converging to each of the three hyperfine thresholds labeled by f_a+f_b. Alternatively this can be viewed as two $a^3\Sigma_u^+$ channels and one $X^1\Sigma_g^+$ channel coupled by the hyperfine interaction. The two $a^3\Sigma_u^+$ channels are distinguished by a different total nuclear spin I. The $f=0$ Hamiltonian consists of only two coupled equations which dissociate to channels $\{f_a,f_b\}$ given by $\{1,1\}$ and $\{2,2\}$. This implies the coupling of one $X^1\Sigma_g^+$ and one $a^3\Sigma_u^+$ channel (see Ref. [31]).

A Hamiltonian block labeled by $\{f,\ell\}$ appears in each full Hamiltonian with total angular momentum F satisfying $|\ell-f|\leq F\leq\ell+f$. However, because these $\{f,\ell\}$ blocks are only weakly coupled to one another, they have essentially identical scattering properties within each Hamiltonian labeled by F. Although we will solve the complete set of coupled differential equations for a given total angular momentum F, we will discuss the physics in terms of the smaller $\{f,\ell\}$ Hamiltonian blocks since they contain all the relevant information. Examination of these $\{f,\ell\}$ Hamiltonians shows that for two ^{39}K$(f_\alpha=1)$ atoms there are two separate scattering lengths—one with $f=2$ and one with $f=0$. We will henceforth refer to these scattering lengths as a_{2s} and a_{0s}. One should note that in principle the three-channel $2s$ Hamiltonian will have three separate scattering lengths corresponding to being at threshold for each of the three asymptotes labeled by f_a+f_b; however, this paper restricts itself to the $f_a=f_b=1$ asymptote and thus we denote $a_{2sf_a=1f_b=1}$ more compactly as a_{2s}. Similar comments hold for the two-channel $0s$ Hamiltonian. The precise value of a_{2s} and a_{0s} depends on the shape of the $X^1\Sigma_g^+$ and $a^3\Sigma_u^+$ potentials which are controlled by the strength of the half-harmonic oscillators. Modifications of the two half-harmonic oscillators smoothly vary the $X^1\Sigma_g^+$ scattering length a_S and the $a^3\Sigma_u^+$ scattering length, a_T. It should be noted that two scattering lengths of importance to Bose-Einstein condensation $a_{2,2}$ for the collision $(f_a=2,m_a=2)+(f_b=2,m_b=2)$ and $a_{1,-1}$ for the collision $(f_a=1,m_a=-1)+(f_b=1,m_b=-1)$, are given by $a_{2,2}=a_T$ and $a_{1,-1}=a_{2s}$.

C. Dipole matrix element

The final element of the theory required to evaluate Eq. (1) is the transition dipole matrix elements $\langle\phi_{p'I'\beta}^{F'v}|\hbar\Omega|\Psi_{Fp\ell f\alpha}^{E(+)}\rangle$ occurring in the numerator of the line shape expression in Eq. (1). Three steps are required in order to evaluate these matrix elements. First, we must obtain the numerical excited bound state and ground state scattering wave functions for each total angular momentum and parity. These are found as described above and are defined on a spatial numerical grid using basis sets that describe all internal and angular momentum degrees of freedom. Second, we must evaluate the Rabi matrix elements between the ground and excited state basis sets. Finally, the numerical bound-free matrix element must be evaluated by integrating over the internuclear separation R. This can be done either by using a direct numerical propagator for the matrix elements while the ground state wave function is being calculated, or by standard numerical quadrature with prestored wave functions. We have tested both methods, and find they give equivalent results.

The molecular Rabi matrix $\mathbf{\Omega}$ between the basis sets for the rotating molecule with hyperfine structure give the matrix elements of the matter-light interaction operator $-\boldsymbol{\varepsilon}\cdot\boldsymbol{d}$, where $\boldsymbol{\varepsilon}$ is the electric vector of the laser field and $\boldsymbol{d}$ is the molecular dipole operator. Thus, Ω is proportional to the square root of the laser intensity, which we assume to be sufficiently weak that there is no power broadening or light shifts. In order to evaluate the Rabi matrix, it is most convenient to express the ground and excited state wave functions in the same type of basis. We use here the separated atom basis $\{(f_af_b)f\ell F\}$ for the ground state and $\{(j_a'f_a'f_b')f'\ell'F'\}$ for the excited state, since for an asymptotically allowed transition the Rabi matrix element is diagonal in ℓ [32]. However ℓ is normally not a good quantum number for an excited eigenstate, and therefore the eigenstates are a linear combination of the $\{(j_a'f_a'f_b')f'\ell'F'\}$ basis states. We have verified that for these excited eigenstates the molecular Rabi matrix reproduces the measured molecular line widths. Notice that these basis sets which include nuclear spin are analogous to a Hund's case (e) basis for atoms without nuclear spin.

The natural selection rules $F'=\{F,F\pm1\}$ and $p=-p'$, mentioned earlier, are inherent to the transition dipole moment. For the 1_u symmetry additional selection rules can be found based on the observation that in the absence of the hyperfine interaction the dipole matrix element only allows transitions from $g\rightarrow u$ and vice versa and that the total nuclear spin and the nuclear mechanical angular momentum in the transition are unchanged. It then follows for $(f_a=1)+(f_b=1)$ scattering that the $0s$ scattering state exists for $F=0$ and $p=+1$ and can only be excited to the $F'=1$, $I'=0$ 1_u line. On the other hand the $2s$ state, which exists for $F=2$ and $p=+1$, can be excited to the $F'=\{1,2,3\}$, $I'=2$ lines. More generally it can be derived that for even ℓ the $f=0$ scattering states can only be excited to 1_u $I'=0$ states and the $f=2$ scattering states are excited to 1_u $I'=2$ states. For odd ℓ the $f=1$ scattering states connect to $I'=1$ 1_u states.

Although the transition dipole moment is a matrix element between multicomponent wave functions, it has properties that are very similar to those of the radial overlap integral that gives the Franck-Condon factor between the ground scattering and excited vibrational wave functions in a conventional two-state picture. Thus, we can use the insights offered by the reflection approximation [16] to aid in our interpretation of the line shapes. In this approximation the dominant contribution to the photoassociation Franck-Condon factor for a single ground and excited state is associated with the amplitude of the ground state wave function at the Condon point for the transition. Thus, if there is a zero in the scattering wave function near the Condon point, where

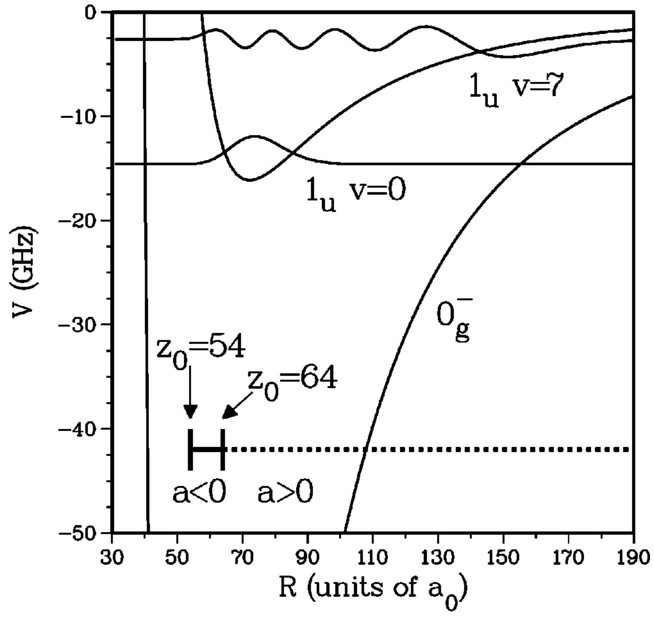

FIG. 2. The long-range adiabatic 1_u potential as a function of internuclear separation. The long-range adiabatic 0_g^- potential is shown for comparison. The zero of energy is at the hyperfine barycenter of the $^2P_{3/2}+^2S$ limit. The 1_u vibrational wave functions for $v=0$ and $v=7$ are shown. Their binding energy is indicated by the intersection of the wave function with the potential energy axis. Also shown is the behavior of the last node z_0 of the zero-energy ^{39}K collision wave function as a function of its scattering length a. For positive a's the last node lies on the dotted line while for negative a's the last node lies on the full line between $54a_0$ and $64a_0$.

the laser is resonant with the difference between ground and excited molecular potentials near the turning point of a vibrational bound state, then that specific vibrational state will have a very small Franck-Condon factor. Although this approximation was developed for the case of a single Condon point at the outer classical turning point for vibrational motion, it still provides a good qualitative guide even for the 1_u state, which has two Condon points, since the Franck-Condon factor predominately comes from the outer turning point. Even $v=0$ would have a small Franck-Condon factor if there were a ground state node in the region of $v=0$ motion.

IV. RESULTS

Figure 2 shows the hyperfine and rotationless Movre-Pichler purely long-range K_2 1_u potential and 1_u vibrational wave functions of the lowest, $v=0$, and the highest, $v=7$, experimentally observed levels. The K_2 1_u curve has a minimum at $72.09a_0$ and a well depth (D_e) of 16.2 GHz. The extent of the vibrational wave functions shows that our experiment is sensitive to a finite range of internuclear separations that is bounded by the inner turning point of the $v=0$ vibrational wave function at $66a_0$ and the outer turning point of the $v=7$ vibrational level at approximately $170a_0$. The inner turning points for $v>0$ are at shorter internuclear separations than that of $v=0$. However, the reflection approximation [16] shows that contributions to the Franck-Condon factors from these inner turning points are typically small.

The intensities of photoassociative lines are sensitive not only to the range of the vibrational wave functions in the excited state, but also to the location of the nodes in the ground state scattering wave function. Franck-Condon factors can oscillate with vibrational quantum number, due to the nodal structure in the ground state wave functions. This oscillatory behavior was seen in the first theory paper on ultracold photoassociation for Na [17] and observed in ^{87}Rb [6] and ^{7}Li [33] photoassociation. As discussed above in Sec. III C, the reflection approximation [16] accounts for this sensitivity to ground state nodes: the existence of a ground state node close to the outer classical turning point for excited state vibrational motion implies a small Franck-Condon factor for the transition.

The horizontal line near the bottom of Fig. 2 schematically shows the position of the ''last'' node [34] z_0 of the ^{39}K zero-energy continuum wave function as a function of its scattering length. The line is based on the theory given in Ref. [13] (see also the Appendix), which gives an exact description of the long-range shape of the s-wave zero energy wave function that is solely based on a pure long-range $1/R^6$ potential and is equally valid for $f=0$ and $f=2$ s-wave scattering. From $C_6=3812.5$ Hartree a_0^6 for ^{39}K [27] we find that the last node of the continuum wave function satisfies $z_0>54a_0$. Other nodes of the wave function can only occur at shorter internuclear separation (a potential with N bound states will have $N-1$ nodes prior to the last one z_0). This also justifies the initial assumption of a pure $1/R^6$ dispersion interaction as exchange and higher-order corrections modify the potentials at much shorter internuclear separations. In addition it can be derived that a node in the dotted region between $64a_0$ and infinity corresponds to a positive scattering length while for $54<z_0<64a_0$ the scattering length is negative. A zero scattering length corresponds to a node at $64a_0$ and an infinite scattering length with a node at $54a_0$.

For ^{39}K the connection between the nodal structure and the dipole matrix elements implies that if the last node of the s-wave wave function is in the range of $66a_0$ to $\approx 170a_0$ it should have a marked effect on the 1_u spectra. This range of nodal positions corresponds to a scattering length between 13 and $\approx 170a_0$. In other words, as long as the scattering length is positive and for a long-range van der Waals potential there is a 75% probability for this to be true (see the Appendix), the K_2 1_u state should provide an ideal state for observing this last node. However, if the scattering length should be negative the last node will be between $54a_0$ and $64a_0$, a range of internuclear separations R which are not well probed by the 1_u photoassociation spectra. For comparison Fig. 2 also shows the purely long-range K_2 0_g^- state. It has a depth of 194.7 GHz and a minimum at $52.23a_0$. Similar arguments on the effect of the nodal structure on the line shapes of 0_g^- features apply.

Based on the simple arguments presented in the above paragraphs the purely long-range 1_u and 0_g^- states appear to be ideal for observing the last node in the s-wave scattering wave function and thereby determining the two observable s-wave scattering lengths. The analysis of the 0_g^- spectrum is given in the accompanying paper [21]. One of the hoped for advantages of using the 1_u over the 0_g^- state is that its resolvable hyperfine structure [10] will provide for a better

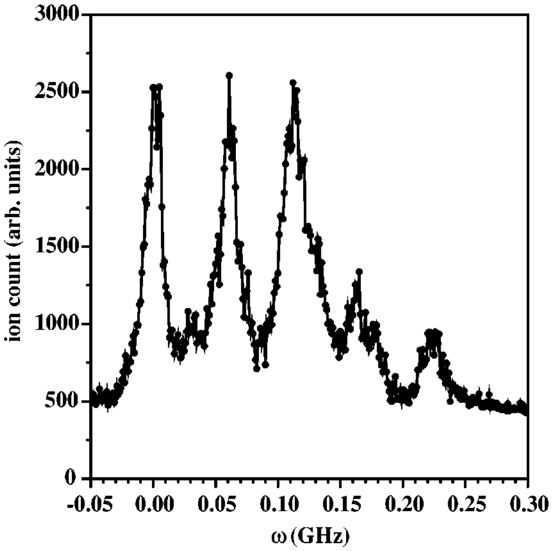

FIG. 3. A typical experimental ionization spectrum for the 1_u $v=0$ vibrational level as a function of laser frequency. The zero of the figure is arbitrarily chosen to coincide with the resonance position of the first line.

disentanglement of the various ground state partial waves ℓ and total hyperfine angular momentum f. As was shown in Tiesinga *et al.* [13] the $J=2$ peak of the rotation dominated 0_g^- spectra receives its intensity predominantly from ground state s-wave collisions. However, because of the lack of observable hyperfine structure in the 0_g^- state it is difficult to separately observe the nodes of both the $2s$ and $0s$ wave functions.

A. Experimental data

Figure 3 presents a typical photoassociation spectrum for $v=0$ of the 1_u state. The actual signal is produced by using a second laser tuned to photoionize the K_2 1_u molecules produced by the photoassociation laser. Thus this is an example of two-color photoassociative ionization where only the photoassociation laser is being scanned. The K_2 1_u spectra shows 6 or 7 major features as compared to the five ($J=0-4$) rotational features observed in the K_2 0_g^- photoassociation spectrum. It has been checked experimentally that power broadening due to the photoassociation laser is negligible. This is, for example, confirmed by the 15 MHz FWHM width of the first features which is in quantitative agreement with a natural linewidth of 7.2 MHz plus a thermal broadening of $k_BT/h\approx 7$–8 MHz.

The left or red-most peak in Fig. 3 is well separated from other features; following Ref. [10] it contains a single hyperfine state labeled by $F'=3$, $I'=2$. From the dipole selection rules it then follows that ground state $f=2$ s- and d-wave collisions contribute to the intensity of this line. However, the asymmetry of the line is consistent with predominantly s-wave scattering [23]. An examination of the $v=1$ through $v=7$ spectra shows that all vibrational levels possess a very similar intensity pattern and in no case is there a significant drop in the relative intensity of the left red-most feature. This suggests that the $2s$ scattering wave function does not have a node between $66a_0$ and $170a_0$ and hence a_{2s} must either be greater than $\approx 170a_0$ or less than $13a_0$.

The only p-wave feature that is experimentally resolved is the small peak or hump in Fig. 3 at 0.03 GHz located between the first two large features. This peak corresponds with a $F'=2$ $I'=1$ 1_u line. For higher vibrational levels this feature slowly increases its relative line strength. Nevertheless this p-wave feature remains weaker than the s-wave features, especially for the lower vibrational levels with turning points that lie inside the p-wave centrifugal barrier at 300 μK and $R=150a_0$.

The right or blue-most feature in Fig. 3 is again well separated from other features. The line is more symmetric than the red-most feature which suggests that it is not due to s-wave scattering. Moreover, for the lines on the blue side of the spectrum the rotational interaction starts to dominate the hyperfine interactions and the lines are approximately described by $J=3$ where $\mathbf{J}=\boldsymbol{\ell}+\mathbf{S}+\mathbf{L}$. A close look at the dipole moment selection rules then shows that contributions of s- and p-wave scattering to $J=3$ 1_u line intensities are nearly absent. Hence this feature primarily obtains intensity from ground state $f=0$ or 2, d-wave collisions. We eliminate contributions from $f=2$ d-wave collisions since the left or red-most peak, which in principle also has contributions from $f=2$ d-wave collisions has a lineshape suggestive of purely s-wave scattering. Thus we assign this blue-most feature as due to $f=0$ d-wave scattering.

The observed line intensity, nevertheless, is anomalously high given a 400 μK thermal distribution of ^{39}K atoms and a d-wave barrier of 1500 μK. This indicates the presence of a d-wave shape resonance. The anomalously large $f=0$ d-wave feature at the blue side of the $v=0$ 1_u spectrum is confirmed by the analysis of the K_2 0_g^- spectrum [21].

The remaining features of Fig. 3 are composed of multiple hyperfine lines and have contributions from $\ell=0,1,2$ scattering. For example, the second strong feature at 0.060 GHz contains two hyperfine lines. One is the $F'=1$, $I'=0$ line formed from $0s$ and $0d$ scattering and the other is a $F'=2$, $I'=2$ line which is accessible from both $2s$ and $2d$ scattering.

B. Consequences for ground-state collisions

In order to show the constraints that the absence of an s-wave node and the existence of a d-wave shape resonance places on the scattering lengths we show in Fig. 4 the scaled scattering length for a_{2s} as a function of the scattering lengths for the singlet and triplet potentials, which were varied as described in Sec. III B. The figure plots the scaled a_{2s} scattering length versus the scaled a_S and a_T scattering lengths. The scaled scattering lengths are defined by the mapping function $A_\gamma=(2/\pi)\arctan(a_\gamma/a_{\mathrm{scale}})$, where γ is $\{S,T,2s\}$ and $a_{\mathrm{scale}}=63a_0$ is the mean scattering length for a collision between two ^{39}K atoms [35] (see the Appendix). Scaled scattering lengths are preferable for plotting since they only vary between $+1$ and -1 while the actual scattering lengths vary between $-\infty$ and $+\infty$. The figure also shows the contour lines for a $2s$ scattering length of $13a_0$ and $170a_0$. These contours define excluded regions (bounded to the left by the $13a_0$ contour and to the right by the $170a_0$

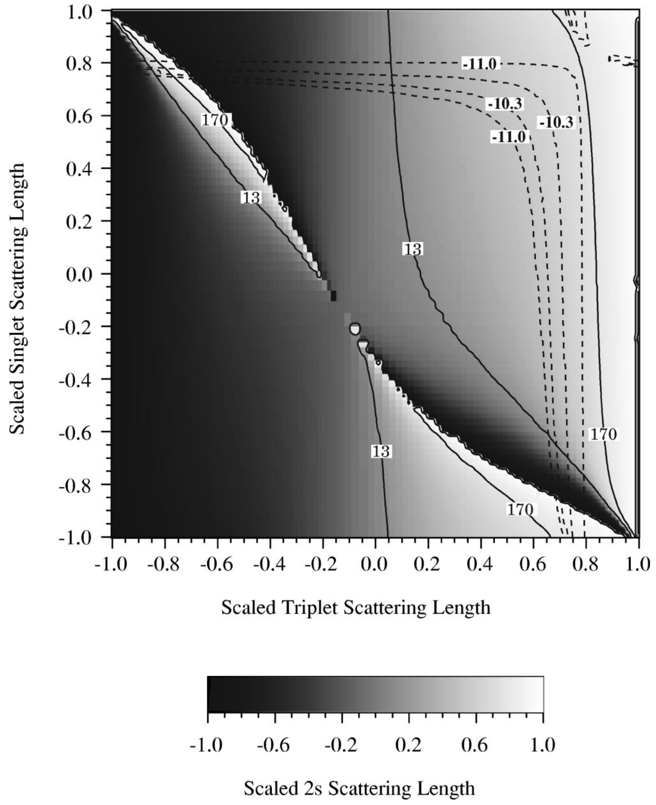

FIG. 4. The scaled a_{2s} scattering length as a function of the scaled $X^1\Sigma_g^+$ and $a^3\Sigma_u^+$ scattering lengths. The full lines correspond to $a_{2s}=13a_0$ or $170a_0$. The dotted lines define a region in the a_{2s} topological map where a $f=0$ d-wave shape resonance affects the 1_u spectra. A precise definition of all lines is given in the text.

contour) that follow from the absence of a reduction in the intensity of the first feature in the spectra for all observed vibrational levels.

The general structure of Fig. 4 can be understood from the structure of the $\{f,\ell\}=\{2s\}$ Hamiltonian which consists at short distances of two $^3\Sigma_u^+$ states and one $^1\Sigma_g^+$ state. The scattering length changes from $+\infty$ to $-\infty$ when the potential is changed such as to cause the removal of one bound state. In essence the behavior of the scattering length has a singularity when a bound state is removed. At the lowest hyperfine asymptote, $(f_a=1)+(f_b=1)$, removing a bound state from the $^3\Sigma_u^+$ state, i.e., causing a_T to jump from $+\infty$ to $-\infty$ or in the scaled coordinates connecting the value 1 to -1, will on average cause the removal of two bound states from the $\{2s\}$ Hamiltonian since it consists of two $^3\Sigma_u^+$ states. Thus, in moving from left to right in the figure the a_{2s} scattering length must have two singularities. One of these occurs on the edges of the figure and the other appears as a Feshbach resonance running from the upper left to the lower right hand corner. A similar change in a_S causes the removal of only one bound state from the $\{2s\}$ Hamiltonian. In moving from the bottom to the top of the figure there is only a single singularity occurring along the diagonal. The value of the a_{2s} scattering length at the very top of the figure is essentially identical with the value vertically below it and at the very bottom of the figure. It is interesting to note that the resonance on the left and right edge of the figure is essentially independent of a_S. Also the Feshbach resonance along the diagonal does not disappear at the center but becomes very narrow at a point where $a_S\approx a_T$, since exchange scattering, which determines the width, is strongly suppressed for the three-channel $\{2s\}$ Hamiltonian along the line where $a_S\approx a_T$ [36–38].

Additionally, Fig. 4 shows contour lines for $\log_{10}K_{0d}^{el}$, the elastic scattering rate constant for $(f_a=1)+(f_b=1)$ collisions for the $\{0d\}$ Hamiltonian at an energy $E/k_B=1500\ \mu\text{K}$ (the top of the d-wave barrier). The four dotted contours from left to right correspond with rate constants of $10^{-11}\ \text{cm}^3/\text{s}$, $5\times10^{-11}=10^{-10.3}\ \text{cm}^3/\text{s}$, $5\times10^{-11}\ \text{cm}^3/\text{s}$, and $10^{-11}\ \text{cm}^3/\text{s}$, respectively. When a shape resonance occurs, K_{0d}^{el} has a relatively sharp maximum at collision energy E_{res}, which defines the ‘‘position’’ of the shape resonance. For (A_T,A_S) pairs between the $5\times10^{-11}\ \text{cm}^3/\text{s}$ contour lines E_{res} is near 1500 μK. For (A_T,A_S) pairs near the two lower contour lines in Fig. 4, E_{res} is smaller than 1500 μK, whereas for (A_T,A_S) pairs near the two upper contour lines, E_{res} is larger than 1500 μK. Consequently, the contours can only be interpreted as locating a region in the a_{2s} plane where the d-wave shape resonance plays a role in the analysis of the photoassociation spectra.

Equivalent contour lines can be found for $(f_a=1)+(f_b=1)$ collisions for the $\{2d\}$ Hamiltonian. It turns out that these $\{2d\}$ curves are nearly identical to the $\{0d\}$ contour lines for $A_S<0.6$ but then turn over at larger singlet scattering lengths, such that the contours cross the line $A_S=1$ near $A_T=-0.1$. The strong experimentally observed d-wave features are consistent with the existence of a shape resonance in the $\{0d\}$ Hamiltonian but inconsistent with a shape resonance in the $\{2d\}$ Hamiltonian. Therefore we need to do a careful search of parameter space in the region of the $0d$ shape resonance but outside the previously excluded region where a_{2s} has values between $13a_0$ and $170a_0$ and outside the region where the $\{2d\}$ Hamiltonian has a shape resonance.

Figure 5 shows the dramatic changes in the calculated $1_u(v=0)$ photoassociation spectra as a_S is adjusted to move across the $f=0$ d-wave resonance region in Fig. 4 at a fixed value of $a_T=-14a_0$ $(A_T=-0.14)$. Between the four simulated spectra the singlet scattering length changes by 20% but the difference between the spectra is marked. It is clear that the curve for $a_S=122a_0$ $(A_S=0.697)$ is unable to explain the experimental data but that the other three spectra show a reasonable agreement. For the spectrum with $a_S=104a_0$ $(A_S=0.653)$ the right most d-wave feature near -14.41 GHz is weakest. In fact, in spectra for $X^1\Sigma_g$ potentials with a smaller a_S, this feature disappears completely. This is consistent with our earlier statements that when the d-wave shape resonance is absent the theory can not explain the observed right-most feature. Thus, the strong sensitivity to the d-wave resonance allows us to put constraints on the range of scattering lengths.

So far, our comparison of the $\text{K}_2 1_u$ $v=0$ calculated and observed photoassociation spectra has led to the above qualitative constraints on the permitted range of variation in the parameters a_S and a_T. Another important consequence of Fig. 5 is that it is essential to construct potentials with a d-wave shape resonance either below the threshold for two $^{39}\text{K}(f_a=1)$ atoms or above the d-wave barrier. An actual

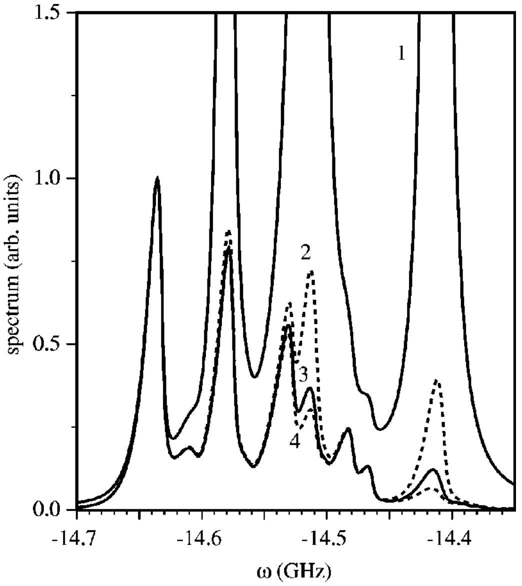

FIG. 5. Theoretical 1_u $v=0$ spectra at $T=400$ μK showing the dramatic effects of the presence of a $\{f\ell\}=\{0d\}$ shape resonance. The frequency scale is relative to the hyperfine barycenter of the $^2P_{3/2}+{}^2S$ limit and all spectra are normalized on the left-most peak. The four spectra are calculated for slightly different $^2S+{}^2S$ potentials. The short-range shape of the $X^1\Sigma_g^+$ potential is varied while the $a^3\Sigma_u^+$ potential stays the same. The triplet scattering length is $a_T=-14a_0$ $(A_T=-0.14)$ for all four spectra while for line 1 (full) $a_S=122a_0$, line 2 (dotted) $a_S=116a_0$, line 3 (full) $a_S=110a_0$, and line 4 (dotted) $a_S=104a_0$. This corresponds with an A_S between 0.653 and 0.697.

resonance between $E/k_B=0$ μK and $E/k_B=1500$ μK leads to *d*-wave features in the photoassociation spectrum that are much stronger than the *s*-wave features. This would be in disagreement with the experimentally observed spectrum. In fact it is only possible to find a very narrow band in the a_S and a_T parameter space below and above the $0d$-shape resonance where qualitative agreement is possible.

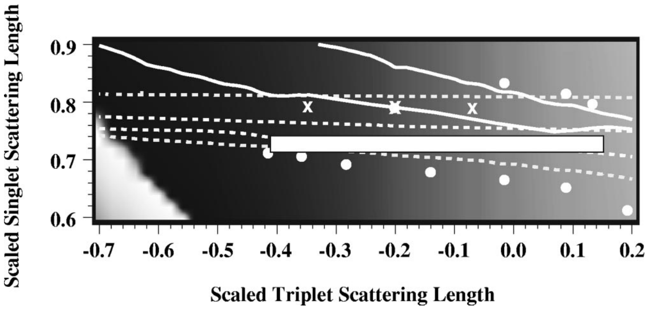

FIG. 6. A blowup of the scaled a_{2s} scattering length as a function of the scaled $X^1\Sigma_g^+$ and $a^3\Sigma_u^+$ scattering lengths. The scaled $a^3\Sigma_u^+$ scattering length lies between -0.7 and $+0.2$ and the scaled $X^1\Sigma_g^+$ scattering length lies between 0.6 and 0.9. The gray scale for the scaled a_{2s} scattering length is identical to that used in Fig. 4. The dotted contour lines define the region in the figure where the $f=0$ d-wave shape resonance modifies the 1_u spectra and the full contour lines define the region of a $f=2$ g-wave shape resonance. The points correspond to ground state potentials that lead to simulated line shapes that agree with the experimental spectrum. The crosses correspond to potentials shown in Fig. 7. The box near $A_S=0.73$ gives the range of allowed A_S and A_T that follow from the 0_g^- line shape analysis [21].

In Fig. 6 we show a blowup of the relevant region of the a_{2s} topological map presented in Fig. 4. The dotted $\log_{10}K_{0d}^{el}$ contour lines which were presented in Fig. 4 are also shown. In addition this figure shows a contour line (full line) for $\log_{10}K_{2g}^{el}$, the elastic scattering rate constant for $(f_a=1)+(f_b=1)$ collisions for the $\{2g\}$ Hamiltonian at an energy $E/k_B=3000$ μK (near the g-wave barrier maximum). The contour corresponds with a rate constant of 10^{-13} cm^3/s and should only be interpreted as locating a region in the a_{2s} plane where a g-wave resonance can be expected. Figure 6 also shows a number of points (white dots) corresponding to values of a_T and a_S where there is reasonable agreement with the $v=0$ experimental spectrum. The points in the figure lying below the $0d$-shape resonance (smaller a_S) correspond to an $\ell=2$ bound state just below threshold, whereas the points lying above the $0d$-shape resonance and to larger a_S correspond to a d-wave resonance just above the d-wave barrier. The region in the figure corresponding to a $2g$ shape resonance must be avoided since it introduces new peaks further to the blue (i.e., to larger total angular momentum) in the theoretical spectra and simultaneously causes some of the observed features to become too large. In Fig. 7 three sample spectra lying near the $0d$ and $2g$ shape resonance show the strong sensitivity to small changes in potentials in this region. In Fig. 7 the three presented spectra are shown as crosses. Finally in Fig. 8 we show a theoretical spectrum corresponding to one of the points (white dots) shown in Fig. 6. Any point along a line connecting the points below the lowest $0d$ contour or a line connecting those above the $0d$ shape resonance in Fig. 6 will provide similar fits. Notice that the middle cross of the three shown in Fig. 6 leads to

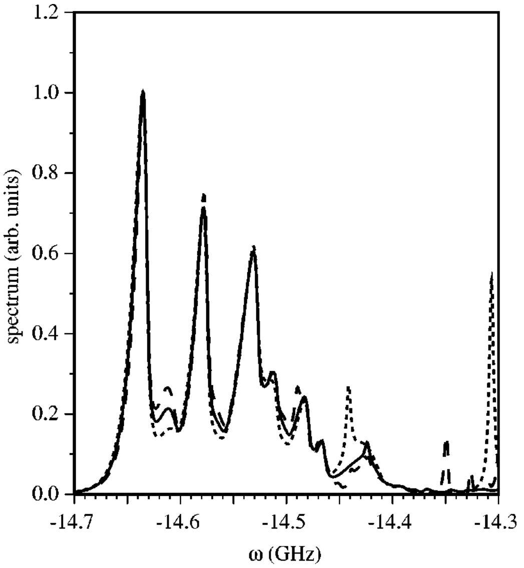

FIG. 7. Theoretical 1_u $v=0$ spectra at $T=400$ μK with $^2S+{}^2S$ potentials that show both $\{f\ell\}=\{0d\}$ and $\{2g\}$ shape resonances. The frequency scale is relative to the hyperfine barycenter of the $^2P_{3/2}+{}^2S$ limit and all spectra are normalized on the left-most peak. The singlet scattering length is $a_S=185a_0$ $(A_S=0.791)$ for all three curves. The dotted line corresponds with $a_T=-7.3a_0$ $(A_T=-0.073)$, the full line corresponds with $a_T=-21a_0$ $(A_T=-0.20)$, and the dashed line corresponds with $a_T=-39a_0$ $(A_T=-0.35)$. The three cases appear as crosses in Fig. 6.

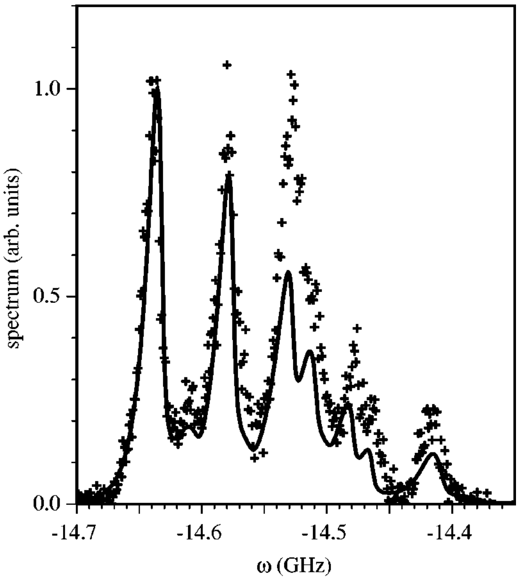

FIG. 8. Comparision between experimental and a typical theoretical 1_u $v=0$ spectra. The frequency scale is relative to the hyperfine barycenter of the $^2P_{3/2}+{}^2S$ limit and all spectra are normalized on the left-most peak. The + signs correspond with the experimental data points and the line with a simulated spectrum at $T=400$ μK. The $X^1\Sigma_g^+$ scattering length is $a_S=110a_0$ ($A_S=0.669$) and the $a^3\Sigma_u^+$ scattering length is $a_T=-14a_0$ ($A_T=-0.14$).

spectra with an acceptable fit to the experimental spectrum. There is a general trend that the small *p*-wave feature that occurs in the experimental spectra between the first two large peaks tends to increase as a_T becomes more negative.

Table I gives the results of our analysis. Note that allowed values of a_S are discontinuous over the quoted range because of the intrusion of the $0d$ shape resonance. However, this does not effect the a_{2s}, a_{0s}, and a_T scattering lengths, which are clearly well constrained. If strong credence is given to the intensity of the *p*-wave feature then the scattering lengths will lie to the more negative end of the values in the table. Changes of C_6 within its 5% uncertainty have only a minor effect on the observable results and does not change the range of scattering lengths. It does cause minor changes in the specific values of a_S but does not change the overall range of a_S values. We extract a temperature of 400 ± 50 μK for the atoms in the MOT. For $T=300$ and 500 μK we find that the left-most feature is noticeably too narrow and too broad respectively.

In our analysis one of the uncertainties lies in the detection scheme. A second photon that creates a more highly excited K dimer can significantly modify the relative line intensities of the photoassociation process [13,10]. Experimentally, this sensitivity is minimized by exciting to a ≈ 1 GHz broad peak below the $\mathrm{K}(5D)+\mathrm{K}(4S)$ limit. In the absence of theoretical modeling of this aspect of the experiment we have to accept simulated spectra where the relative intensities do not match too exactly.

TABLE I. ^{39}K scattering length a_γ in units of a_0 and corresponding scaled scattering lengths A_γ.

$+90<a_S<+230$	$0.61<A_S<0.83$
$-60<a_T<+15$	$-0.48<A_T<0.15$
$-150<a_{2s}<+20$	$-0.75<A_{2s}<0.20$
$+5<a_{0s}<+100$	$0.05<A_{0s}<0.64$

A similar analysis based on the $^{39}\mathrm{K}_2$ 0_g^- photoassociation spectra provides results that are in agreement with those presented here with the exception that the 0_g^- analysis finds a different restricted value of a_S that lies within the range of values we quote but corresponds to having the peak of the $0d$ shape resonance between $E/k_B=800$ μK and $E/k_B=1500$ μK. This requirement is based on obtaining the necessary width for the $J=2$ 0_g^- feature which would be dominated by *s*-wave in the absence of the resonance [21]. The results of Ref. [21] are shown as a box near $A_S=0.73$ in Fig. 6.

Although the analysis of both the 1_u and 0_g^- spectra is basically consistent in requiring a $0d$ shape resonance to explain the observed spectral features, the specific conclusion regarding the resonance position appear to be mutually exclusive over much of the permitted range of a_T, although this difference does not actually lead to any significant differences in the constraints placed on the a_T and a_{2s} scattering lengths which are crucial to BEC studies. The near overlap shown in Fig. 6 of the permitted ranges from the 1_u and 0_g^- analyses near the extreme lower left hand side of the 0_g^- box is suggestive that a_T may lie much closer to $-60a_0$ than $+16a_0$. However, we should note that there may be limitations inherent in the methodology of analyzing photoassociation spectra based on interpreting relative intensities as being due to absorption of the photoassociating light at frequency ν_1. An important subject of future research, both experimental and theoretical, would be to understand better the effect of the ionizing photon at frequency ν_2 on the spectral intensities. Although relatively broad and structureless features are involved in the photoionization step, it is not yet clear how absorption of the ν_2 photon affects the relative shapes and strengths of the experimental spectra.

V. CONCLUSIONS

We have presented a quantitative analysis of the spectra of vibrational levels of the long-range 1_u curve of the $^{39}\mathrm{K}_2$ dimer. High precision photoassociative spectroscopy from ultracold K atoms allowed us to resolve the rotational-hyperfine structure of these vibrational levels. Theoretical modeling had previously enabled some of us [10] to assign the observed hyperfine structure. In this paper we were able to model the lineshape and extract properties of the ground state collision between ^2S ^{39}K atoms held at ultra-cold temperatures in a magneto-optical trap.

The analysis of the intensity spectra showed that no node in *s*-wave scattering wave function can exist between $66a_0$ and $170a_0$. This nodal structure immediately excluded a_{2s} scattering lengths between $+13a_0$ and $170a_0$. We also found that shape resonances play a crucial role in the formation of the excited molecule. The experimental spectra show clear signs of the presence of a *d*-wave shape resonance. In the absence of such a resonance *d*-wave collisions should not have contributed measurably to the spectrum because the 400 μK temperature of the gas is considerably lower than the 1500 μK centrifugal barrier. In addition simulated and measured spectra only agree by narrowly avoiding a *g*-wave resonance in an accessible entrance channel. The interplay of all the shape resonances and exclusion of a range of scattering lengths allowed us to give bounds for the experimentally observable scattering lengths.

The inclusion of constraints resulting from the observation of a *p*-wave resonance in ^{40}K scattering [39] provides further restrictions on the allowed values of a_T. A joint analysis of this data along with the ^{39}K$_2$ 0_g^- analysis [21] will be presented in a future publication.

ACKNOWLEDGMENTS

We thank J.P. Burke, C.H. Green and J.L. Bohn for communicating their theoretical analysis prior to publication. E.T. would like to acknowledge support by the Army Research Office and the work at the University of Connecticut is partially supported by the National Science Foundation.

APPENDIX: LENGTH SCALES

The low energy properties of scattering wave functions and collisional cross sections are to a large extent determined by the long-range shape of the interaction potential. This appendix discusses several length scales relevant for an attractive C_6/R^6 potential. A connection with length scales in existing literature is made.

The simplest length scale is obtained by restating the Schrödinger equation for a pure C_6/R^6 potential in dimensionless units. It follows that it is convenient to introduce a scale $x_0 = \sqrt[4]{2\mu C_6/\hbar^2}/2$. The factor of one half is arbitrary. However, it turns out that, using this base definition x_0 is nearly identical to length scales that are derived from specific physical requirements and which are discussed below.

The first of such physical lengths describes the connection between the last node of the zero-energy wave function and the corresponding scattering length [13]. The discussion around Fig. 2 has already touched on some of these issues. The connection is most relevant for photoassociation spectroscopy with ultra-cold atoms. The line intensities of the spectroscopic features are an image of the zero-energy wave function at the Condon point of the transitions [16] and hence Condon points close to nodes of a wave function lead to disappearing spectral features.

The basic concept behind the connection is that for a given scattering length *a* the long-range form of the radial wave function for zero kinetic energy is obtained by integrating the Schrödinger equation from ∞ to shorter internuclear separations *R*. In fact, this integration is known analytically for $1/R^n$ potentials and yields for $n=6$

$$\sqrt{x}[\Gamma(5/4)J_{1/4}(2/x^2) - \Gamma(3/4)J_{-1/4}(2/x^2)/a] \rightarrow 1 - x/a \quad \text{for} \quad x\rightarrow\infty, \tag{A1}$$

where $x = R/x_0$ and *a* is expressed in units of x_0. This wave function is exact as long as $1/R^6$ is a good representation for the real potential. Equation (A1) immediately describes a relation between the node positions z_0 and the scattering length. For example it follows that, for infinite scattering length $z_0 = 0.848x_0$ from $J_{1/4}(2/z_0^2) = 0$ and for zero scattering length $z_0 = 0.998x_0$ from $J_{-1/4}(2/z_0^2) = 0$. It turns out that typical values of z_0 for alkali-metal dimers always lies at a value *R* of the internuclear coordinate where chemical or exchange contributions to the interaction potential are negligible. As a practical point deviations occur when the electron clouds of the two atoms overlap, which for alkali-metal dimers is somewhere between $20a_0$ and $30a_0$ [40]. As a result the value of x_0 for the Li dimer is close to where the contributions due to exchange are becoming relevant.

A second length scale is due to Gribakin and Flambaum [35]. This scale describes the mean scattering length for a $1/R^6$ potential. Unlike the derivation of z_0 versus *a* the average scattering length is found by integrating from short range to infinity with the restriction that the interatomic potential is described by $-C_6/R^6$ over this range. The integration is started from a given log-derivative of the zero-energy wave function. The precise value of the log-derivative depends on the exact shape of the short-range part of the interatomic potential. An analytic one-to-one correspondence between this log derivative and the scattering length can then be derived. Since all values of the log-derivative are equally likely, the average scattering length is given by averaging over all log derivatives and is equal to $\overline{a} = 0.956x_0$. It also follows that for a $-C_6/R^6$ potential there is a 25% chance of a negative scattering length.

A third length scale is proposed by Julienne and Mies [41]. The length scale highlights the breakdown of the semiclassical Wigner-Kramers-Brillouin (WKB) approximation. The WKB approximation for collisional phase shifts or cross sections is valid when for all internuclear separations the change of the amplitude of the wave function is negligible over a local de Broglie wavelength. For sufficiently small collision energies, however, the WKB approximation breaks down. The change of the wave function amplitude is still small for short and large internuclear separations but peaks in between in such a way that the peak value increases with decreasing collision energy.

Following a more rigorous discussion of the WKB breakdown, Ref. [41] defines a collision energy ϵ_Q and a length scale R_Q for the breakdown of the semi-classical approximation by the requirement that $d\lambda(\epsilon_Q, R_Q)/dR$ has a maximum at R_Q and equals 0.5. Here $\lambda(\epsilon,R) = 2\pi/\sqrt{2\mu/\hbar^2(\epsilon - C_6/R^6)}$ is the local de Broglie wavelength and the interatomic potential is given by a long-range $-C_6/R^6$ dispersion interaction. Some algebra then yields $R_Q = 0.986x_0$.

---

[1] H. M. J. M. Boesten, J. M. Vogels, J. G. C. Tempelaars, and B. J. Verhaar, Phys. Rev. A **54**, R3726 (1996).

[2] R. Côté, A. Dalgarno, H. Wang, and W. C. Stwalley, Phys. Rev. A **57**, R4118 (1998).

[3] R. Côté, A. Dalgarno, and M. J. Jamieson, Phys. Rev. A **50**, 399 (1994).

[4] A. J. Moerdijk, W. C. Stwalley, R. G. Hulet, and B. J. Verhaar, Phys. Rev. Lett. **72**, 40 (1994).

[5] P. D. Lett, K. Helmerson, W. D. Phillips, L. P. Ratliff, S. L. Rolston, and M. E. Wagshul, Phys. Rev. Lett. **71**, 2200 (1993).
[6] J. D. Miller, R. A. Cline, and D. J. Heinzen, Phys. Rev. Lett. **71**, 2204 (1993).
[7] W. I. McAlexander, E. R. I. Abraham, N. W. M. Ritchie, C. J. Williams, H. T. C. Stoof, and R. G. Hulet, Phys. Rev. A **51**, R871 (1995).
[8] H. Wang, P. L. Gould, and W. C. Stwalley, Phys. Rev. A **53**, R1216 (1996).
[9] H. Wang, J. Li, X. T. Wang, C. J. Williams, P. L. Gould, and W. C. Stwalley, Phys. Rev. A **55**, R1569 (1997).
[10] X. Wang, H. Wang, P. L. Gould, W. C. Stwalley, E. Tiesinga, and P. S. Julienne, Phys. Rev. A **57**, 4600 (1998).
[11] A. Fioretti, D. Comparat, A. Crubellier, O. Dulieu, F. Masnou-Seeuws, and P. Pillet, Phys. Rev. Lett. **80**, 4402 (1998).
[12] A. Fioretti, D. Comparat, C. Drag, C. Amiot, O. Dulieu, F. Masnou-Seeuws, and P. Pillet, Eur. Phys. J. D **5**, 389 (1999).
[13] E. Tiesinga, C. J. Williams, P. S. Julienne, K. M. Jones, P. D. Lett, and W. D. Phillips, J. Res. Natl. Inst. Stand. Technol. **101**, 505 (1996).
[14] H. M. J. M. Boesten, C. C. Tsai, B. J. Verhaar, and D. J. Heinzen, Phys. Rev. Lett. **77**, 5194 (1996); H. M. J. M. Boesten, C. C. Tsai, J. R. Gardner, D. J. Heinzen, and B. J. Verhaar, Phys. Rev. A **55**, 636 (1997).
[15] N. Newbury, C. Myatt, and C. Wieman, Phys. Rev. A **51**, R2680 (1995).
[16] P. S. Julienne, J. Res. Natl. Inst. Stand. Technol. **101**, 487 (1996).
[17] H. R. Thorsheim, J. Weiner, and P. S. Julienne, Phys. Rev. Lett. **58**, 2420 (1987).
[18] M. Movre and G. Pichler, J. Phys. B **10**, 2631 (1977).
[19] W. C. Stwalley, Y.-H. Uang, and G. Pichler, Phys. Rev. Lett. **41**, 1164 (1978).
[20] D. Comparat, C. Drag, A. Fioretti, O. Dulieu, A. Crubellier, F. Masnou-Seeuws, and P. Pillet, Eur. Phys. J. D (to be published).
[21] J. P. Burke, C. H. Green, J. L. Bohn, H. Wang, P. L. Gould, and W. C. Stwalley, preceding paper, Phys. Rev. A.
[22] H. Wang, X. T. Wang, P. L. Gould, and W. C. Stwalley, Phys. Rev. Lett. **78**, 4173 (1997).
[23] R. Napolitano, J. Weiner, C. J. Williams, and P. S. Julienne, Phys. Rev. Lett. **73**, 1352 (1994).
[24] Henceforth f denotes the summed angular momentum for the two atoms, whereas f_a and f_b denotes the angular momenta of the individual atoms.
[25] K. M. Jones, P. S. Julienne, P. D. Lett, W. D. Phillips, E. Tiesinga, and C. J. Williams, Europhys. Lett. **35**, 85 (1996).
[26] G. Herzberg, *Spectra of Diatomic Molecules* (van Nostrand, New York, 1950).
[27] M. Marinescu and A. Dalgarno, Phys. Rev. A **52**, 311 (1995).
[28] E. Tiesinga, C. J. Williams, and P. S. Julienne, Phys. Rev. A **57**, 4257 (1998).
[29] H. Lefebvre-Brion and R. W. Field, *Perturbations in the Spectra of Diatomic Molecules* (Academic, New York, 1986).
[30] H. T. C. Stoof, J. M. V. A. Koelman, and B. J. Verhaar, Phys. Rev. B **38**, 4688 (1988).
[31] F. H. Mies, C. J. Williams, P. S. Julienne, and M. Krauss, J. Res. Natl. Inst. Stand. Technol. **101**, 521 (1996).
[32] P. S. Julienne and F. H. Mies, Phys. Rev. A **30**, 831 (1984); **34**, 3792 (1986).
[33] R. Côté, A. Dalgarno, Y. Sun, and R. G. Hulet, Phys. Rev. Lett. **74**, 3581 (1995).
[34] The concept of a last node only applies in the limit of zero energy scattering; at low but finite collision energy, it is the ‘‘last’’ node before the start of the nodes associated with oscillations of the asymptotic $\sin[k(R-a)]$ wave function.
[35] G. F. Gribakin and V. V. Flambaum, Phys. Rev. A **48**, 546 (1993).
[36] P. S. Julienne, F. H. Mies, E. Tiesinga, and C. J. Williams, Phys. Rev. Lett. **78**, 1880 (1997).
[37] J. P. Burke, J. L. Bohn, B. D. Esry, and C. H. Greene, Phys. Rev. A **55**, R2511 (1997).
[38] S. J. J. M. F. Kokkelmans, H. M. J. M. Boesten, and B. J. Verhaar, Phys. Rev. A **55**, R1589 (1997).
[39] B. DeMarco, J. L. Bohn, J. P. Burke, Jr., M. Holland, and D. S. Jin, Phys. Rev. Lett. **82**, 4208 (1999).
[40] W. C. Stwalley, Chem. Phys. Lett. **6**, 241 (1970); R. J. LeRoy and R. B. Bernstein, J. Chem. Phys. **52**, 3869 (1970).
[41] P. S. Julienne and F. H. Mies, J. Opt. Soc. Am. B **6**, 2256 (1989).